ACS Catalysis

Letter

pubs.acs.org/acscatalysis

Enhancing Catalytic CO Oxidation over Co_3O_4 Nanowires by Substituting Co^{2+} with Cu^{2+}

Minjie Zhou,[†,‡,⊥] Lili Cai,[†,⊥] Michal Bajdich,[§] Max García-Melchor,[§] Hong Li,[†] Jiajun He,[∥] Jennifer Wilcox,[∥] Weidong Wu,[*,‡] Aleksandra Vojvodic,[§] and Xiaolin Zheng[*,†]

[†]Department of Mechanical Engineering, [∥]Department of Energy Resources Engineering, Stanford University, Stanford, California 94305, United States

[‡]Research Center of Laser Fusion, CAEP, P.O. Box 919-987-7, Mianyang 621900, People's Republic of China

[§]SUNCAT Center for Interface Science and Catalysis, SLAC National Accelerator Laboratory, 2575 San Hill Road, Menlo Park, California 94025, United States

Supporting Information

ABSTRACT: Co_3O_4 is an attractive earth-abundant catalyst for CO oxidation, and its high catalytic activity has been attributed to Co^{3+} cations surrounded by Co^{2+} ions. Hence, the majority of efforts for enhancing the activity of Co_3O_4 have been focused on exposing more Co^{3+} cations on the surface. Herein, we enhance the catalytic activity of Co_3O_4 by replacing the Co^{2+} ions in the lattice with Cu^{2+}. Polycrystalline Co_3O_4 nanowires for which Co^{2+} is substituted with Cu^{2+} are synthesized using a modified hydrothermal method. The Cu-substituted Co_3O_4_Cu*x* polycrystalline nanowires exhibit much higher catalytic activity for CO oxidation than pure Co_3O_4 polycrystalline nanowires and catalytic activity similar to those single crystalline Co_3O_4 nanobelts with predominantly exposed most active {110} planes. Our computational simulations reveal that Cu^{2+} substitution for Co^{2+} is preferred over Co^{3+} both in the Co_3O_4 bulk and at the surface. The presence of Cu dopants changes the CO adsorption on the Co^{3+} surface sites only slightly, but the oxygen vacancy is more favorably formed in the bonding of Co^{3+}–O–Cu^{2+} than in Co^{3+}–O–Co^{2+}. This study provides a general approach for rational optimization of nanostructured metal oxide catalysts by substituting inactive cations near the active sites and thereby increasing the overall activity of the exposed surfaces.

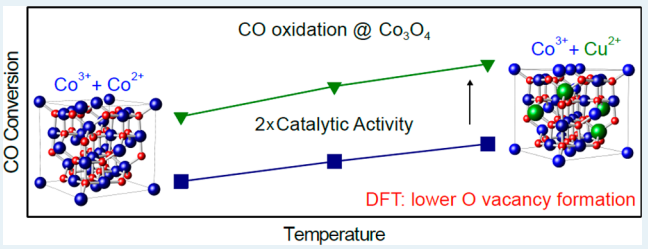

KEYWORDS: *Co_3O_4, nanowire arrays, catalytic CO oxidation, Cu doping, surface activity*

INTRODUCTION

Carbon monoxide (CO) emission from transportation and industrial activities is harmful to both human health and the environment. Currently, CO emission is effectively reduced, mainly through catalytic oxidation over catalysts.[1−4] The most active catalysts for CO oxidation are noble metals, but they are expensive and are of limited supply. Co_3O_4 has emerged as an attractive alternative catalyst for CO oxidation because of its optimal CO adsorption strength, low barrier for CO reaction with lattice O, and excellent redox capacity.[1,5−8] A breakthrough on Co_3O_4 for catalytic CO oxidation showing that Co_3O_4 nanorods with predominantly exposed {110} planes exhibit a much higher catalytic activity for CO oxidation and larger resistance to deactivation by water than Co_3O_4 nanoparticles was reported by Xie et al.[9] The high catalytic activity of Co_3O_4 {110} planes is attributed to its higher concentration of Co^{3+} cations (correspondingly fewer Co^{2+} cations) than other crystal planes, since only Co^{3+} cations surrounded by Co^{2+} ions are active for catalytic oxidation of CO.[10,11] Subsequently, a number of Co_3O_4 nanostructures, ranging from nanobelts, nanospheres, nanocubes, and nanotubes to nanowires, have been synthesized with the purpose of preferentially exposing Co^{3+} cations.[11−14] Nevertheless, regardless of the morphology of the Co_3O_4 nanostructures, even the highly active Co_3O_4 {110} planes still contain Co^{2+} cations, which have been assumed to be inactive for catalytic oxidation of CO,[9−11] and ultimately limits the catalytic activity of Co_3O_4 for CO oxidation. Therefore, substituting Co^{2+} with other divalent cations that are active for CO oxidation presents a new opportunity to further improve the catalytic activity of Co_3O_4. In this regard, Cu^{2+} is an ideal candidate for substituting Co^{2+} in the Co_3O_4 lattice because the Cu^{2+} cation not only is active for CO oxidation,[1,15,16] but also has an ionic radius that is similar to that of the Co^{2+} cation (Figure 1). In addition, replacing Co^{2+} with Cu^{2+} could also modify the intrinsic activity of Co^{3+} by changing the bonding environment surrounding Co.[8,17−21]

In this study, we show that replacing Co^{2+} with Cu^{2+} cations in polycrystalline Co_3O_4 nanowires greatly enhances their catalytic activity for CO oxidation. The Co^{2+} cation

Received: March 8, 2015
Revised: June 16, 2015
Published: June 22, 2015

DOI: 10.1021/acscatal.5b00488
ACS Catal. 2015, 5, 4485−4491

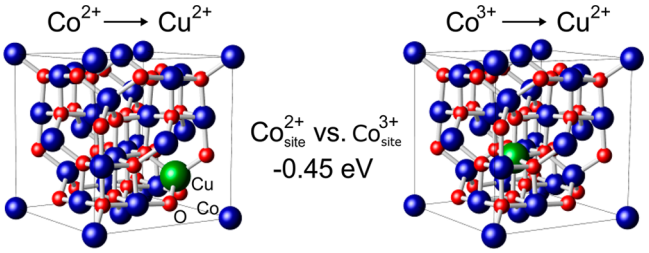

Figure 1. Bulk structure of spinel Co_3O_4 with single tetragonal Co^{2+} cations (left) and single octahedral Co^{3+} (right), being replaced by Cu^{2+} cations. The indicated energy is the total energy difference between the two illustrated structures. It illustrates that Co^{2+}, not Co^{3+}, will be preferentially replaced by Cu^{2+}.

replacement was realized by introducing a Cu^{2+} precursor during the hydrothermal synthesis process of Co_3O_4 nanowires and the preferred energetics of substituting Cu for Co^{2+} over Co^{3+} was established from atomistic modeling. The amount of Cu^{2+} precursor was varied during the synthesis of Co_3O_4, and the catalytic activity was found to increase with the amount of exchanged Cu^{2+} for Co^{2+} ions in the polycrystalline Co_3O_4 nanowires, provided phase segregation was avoided. Density functional theory simulations find that the reactivity of the Cu-doped Co_3O_4 surfaces changes in a favorable way toward CO adsorption and O vacancy formation. Taken together, these results show that substitution of Co^{2+} ions with isovalent Cu^{2+} ions provides an effective route to improve the catalytic activity of Co_3O_4.

EXPERIMENTAL SECTION

Co_3O_4 nanowires, for which Co^{2+} is partially replaced with Cu^{2+}, are referred to here as Co_3O_4_Cu*x* nanowires, and they were grown on stainless steel (SS) meshes by a hydrothermal method based on a reported recipe, with modification.[22] Briefly, an aqueous solution was prepared by mixing 60 mmol of urea and 100 mL of deionized (DI) water with agitation in a beaker. Then a fixed amount of 10 mmol $Co(NO_3)_2{\cdot}6H_2O$ with different amounts of $Cu(NO_3)_2{\cdot}4H_2O$ (0, 1.25, 2.5, or 3.75 mmol) was dissolved in the aqueous solution. The resulting catalysts are noted as Co_3O_4_Cu0, Co_3O_4_Cu1, Co_3O_4_Cu2 and Co_3O_4_Cu3, respectively (Table 1). The solution was magnetically stirred for 10 min in air and subsequently transferred to a Teflon-lined autoclave. A piece of 2 in. × 12 in. SS mesh (0.0055 in. wire diameter and 0.02 in. opening size; McMaster-Carr) was rolled up to a cylindrical shape with 2 in. length and 0.7 in. diameter, and this SS mesh cylinder was placed into the autoclave as the growth substrate for the Co_3O_4_Cu*x* nanowires. The autoclave with the mixture was then kept in an oven at 120 °C for 6 h for the growth of Cu-alloyed Co_3O_4 nanowires. After the growth, the samples were thoroughly rinsed with DI water and dried at 70 °C for 2 h. Finally, the samples were annealed in air at 450 °C for 4 h.

The morphology and crystallinity of the Co_3O_4_Cu*x* nanowires were examined by scanning electron microscopy (SEM; FEI XL30 Sirion) and X-ray diffraction (XRD; PANalytical XPert), respectively. The chemical composition and oxidation states of the nanowires were further examined by X-ray photoelectron spectroscopy (XPS, SSI S-Probe). Decomposition of XPS peaks was carried out to examine the peak fine structures, for which the common XPS peak fitting methods Shirley background and a mixed Gaussian−Lorentzian peak profile were applied.[23] The detailed microstructure of the nanowires was studied by transmission electron microscopy (TEM; FEI Tecnai F20). The elemental analysis of the nanowires was performed using SEM and scanning TEM (STEM) in conjunction with energy-dispersive X-ray spectroscopy (EDX). The TEM samples were prepared by removing the nanowires from the SS mesh, dispersing them into alcohol, and then dropping them onto a lacey-carbon-film-supported Au TEM grid. It should be noted that Au TEM grids instead of Cu grids were used to prevent the Cu signal from the Cu TEM grid from affecting the EDX measurement of the Cu distribution in Co_3O_4_Cu*x* nanowires. The specific surface areas of the Co_3O_4_Cu*x* nanowires were obtained by the Brunauer−Emmett−Teller (BET) method, for which the nitrogen sorption analysis of all the Co_3O_4_Cu*x* nanowires (removed from the SS mesh) was performed using 99.999% pure nitrogen gas at 77 K in an Autosorb iQ2 low-pressure gas sorption analyzer (Quantachrome).

The catalytic activity of the Co_3O_4_Cu*x* nanowires for CO oxidation was measured in an in-house-built tube flow reactor. The reactor consists of a quartz tube (90 cm in length, 2 cm in i.d.) housed in a tube furnace (Lindberg, Blue M Mini-Mite). The inflow was a mixture of 2.0 vol % CO and 3.0 vol % O_2 diluted in helium, with a total flow rate of 120 sccm. The flow rates of all the gases were controlled by mass flow controllers (Horiba Z500). The effluent gas was connected to a gas chromatograph (SRI Multiple Gas Analyzer) directly for composition analysis. For all the experiments, CO_2 was the only CO oxidation product detected, and the difference of total carbon mole fraction between the effluent and inflow gases was <0.1%, indicating that CO is converted to CO_2 only. Hence, the CO conversion percentage is calculated by

$$\mathrm{CO\%} = \frac{X_{CO_2}}{X_{CO_2} + X_{CO}}$$

Table 1. Compositions of the Growth Precursor Solutions for the Four Co_3O_4_Cu*x* Samples and Their Respective Total Mass Loading, Specific Surface Area, Total Surface Area[a] Obtained by the BET Analysis, and Cu/Co Atomic Ratio Measured by SEM-EDX

	growth precursor solution						
sample	$Co(NO_3)_2{\cdot}6H_2O$ (10^{-3} M)	urea (10^{-3} M)	$Cu(NO_3)_2{\cdot}4H_2O$ (10^{-3} M)	total mass loading (mg)	S_{BET} (without substrate)(m^2/g)	total surface area (m^2)	Cu/Co atomic ratio measured by EDX, %
Co_3O_4_Cu0	100.0	600.0	0.0	240	23	5.5	0.0
Co_3O_4_Cu1	100.0	600.0	12.5	229	25	5.7	11.5
Co_3O_4_Cu2	100.0	600.0	25.0	215	27	5.8	15.6
Co_3O_4_Cu3	100.0	600.0	37.5	240	22	5.3	29.5

[a]All without including the SS mesh.

DOI: 10.1021/acscatal.5b00488
ACS Catal. 2015, 5, 4485−4491

where X_{CO_2} and X_{CO} are the molar percentages of CO_2 and CO in the effluent gas measured by the gas chromatograph.

RESULTS AND DISCUSSION

Figure 2a,b shows that the color of the SS mesh cylinder changes from bright silver to dark black after the hydrothermal growth, indicating the successful growth of Co_3O_4_Cu*x*-based catalysts. SEM images (Figure 2c,d,e) confirm that dense nanowire arrays are grown uniformly over the entire surface of the SS mesh. Regardless of the Cu^{2+} concentration, the final Co_3O_4_Cu*x* nanowires have similar dimensions, with an average length and diameter of 5 μm and 70 nm, respectively, similar to those of Co_3O_4_Cu2 shown in Figure 2f (top view) and g (side view). TEM images further confirm that the morphologies of pure Co_3O_4_Cu0 nanowire and Cu alloyed Co_3O_4_Cu*x* nanowires are similar (Figure 3a,b), and both are polycrystalline, as evidenced by the multiple bright diffraction rings in the selected area electron diffraction (SAED) pattern (Figure 3c). The high-resolution TEM image (Figure 3d) of Co_3O_4_Cu2 nanowire shows that the interplanar distances are 0.24 and 0.29 nm, which could be indexed as the interplanar distances of the Co_3O_4 (311) and (220) planes, respectively. We also note that the lattice parameters for Co_3O_4 and $Co_{3-x}Cu_xO_4$ are very similar, so the chemical composition of the nanowires was further examined by SEM-EDX and STEM-EDX elemental analysis. For each sample, we took 10 measurements at different spots using SEM-EDX and calculated the average values of the Cu/Co atomic ratio, as listed in Table 1. It can be found that the Cu concentration in the Co_3O_4_Cu*x* nanowires increases with that in the growth precursor. For the Cu-alloyed Co_3O_4_Cu2 nanowires, the elemental distributions of Co and Cu along the radial direction (marked by the red line in the STEM dark field image in Figure 3e) measured by STEM-EDX have similar profiles (Figure 3f), confirming the successful incorporation of Cu into the nanowires. Moreover, the incorporation of Cu^{2+} ions was also investigated by means of DFT+U calculations (see Supporting Information for details). We find that replacing a Co^{2+} ion with Cu^{2+} in the bulk Co_3O_4 is favored by 0.45 eV compared with the substitution of a Co^{3+} ion (Figure 1). This is in agreement with the experimentally observed substitution of Co^{2+} in Co_3O_4 with Cu^{2+}, explained in more detail below.

The crystallinity and phase of the Co_3O_4_Cu*x* nanowire arrays were further examined by XRD (Figure 4). When the amount of Cu incorporation is moderate, the XRD patterns of sample Co_3O_4_Cu*x* (x = 1 and 2) are almost identical to pure Co_3O_4_Cu0 and the standard Co_3O_4 reference, which suggests that the alloyed Cu^{2+} cations in sample Co_3O_4_Cu1 and

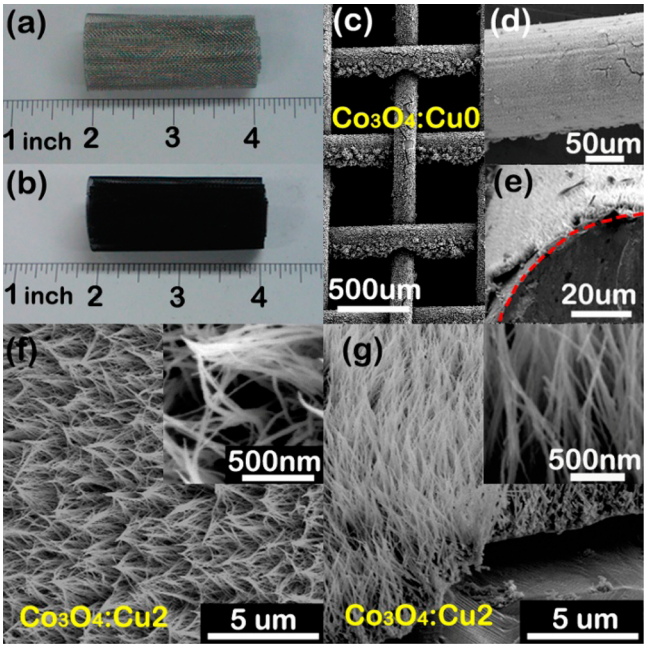

Figure 2. Photographs of the SS mesh cylinder (a) before and (b) after the growth of Co_3O_4_Cu*x* nanowires. SEM images of (c) Co_3O_4_Cu0 nanowires with (d) enlarged plane view and (e) cross-sectional view. SEM images of the (f) top view and (g) side view of Co_3O_4_Cu2 nanowires with insets for higher magnification images.

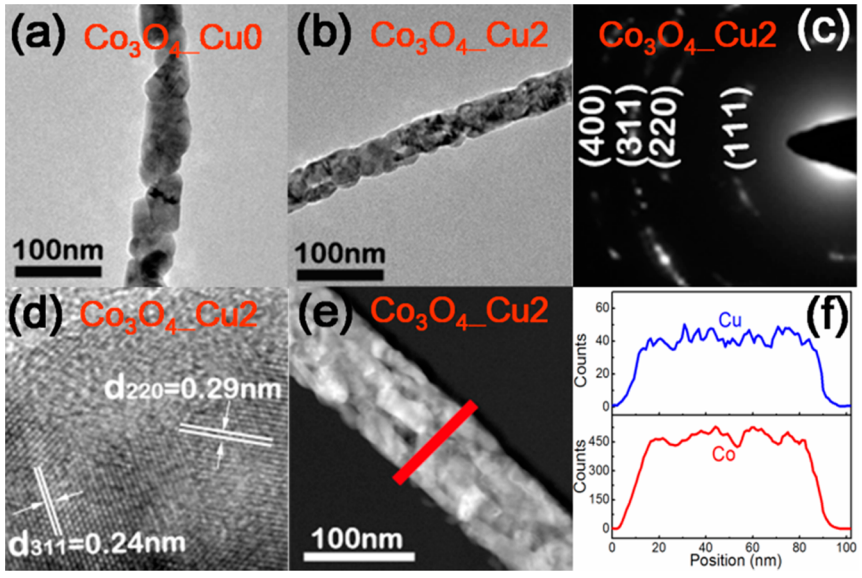

Figure 3. Low-magnification TEM images of (a) Co_3O_4_Cu0 and (b) Co_3O_4_Cu2 nanowires; (c) SAED pattern, (d) high resolution TEM image, (e) STEM dark field image, and (f) elemental line scan profile of Co_3O_4_Cu2 nanowires.

DOI: 10.1021/acscatal.5b00488
ACS Catal. 2015, 5, 4485−4491

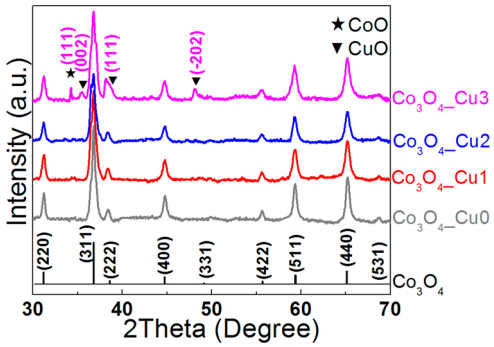

Figure 4. XRD spectra of Co_3O_4_Cu0, Co_3O_4_Cu1, Co_3O_4_Cu2, and Co_3O_4_Cu3 nanowires and the standard cubic Co_3O_4 reference.

Co_3O_4_Cu2 mainly substitute for the Co^{2+} cations in the Co_3O_4 lattice without a measurable amount of phase segregation. Nevertheless, for Co_3O_4_Cu3 nanowires, for which the Cu^{2+} concentration in the growth precursor solution is higher, additional peaks corresponding to CoO (111) (JCPDS PDF 42-1300) and CuO (002), (111), (−202) (JCPDS PDF 80-1917) appear in the XRD pattern. This indicates that a higher Cu^{2+} concentration in the precursor solution leads to a significant phase separation. Hence, only Co_3O_4_Cu1 and Co_3O_4_Cu2 nanowires are the desired Co_3O_4 for which Co^{2+} is substituted with Cu^{2+}.

The oxidation states of Co and Cu cations on the surface of the Co_3O_4_Cu*x* nanowire arrays were examined by XPS measurements. The two fitted peaks for Co $2p_{3/2}$, that is, Co^{3+} (~779.6 eV) and Co^{2+} (~781.0 eV), for both Co_3O_4_Cu0 (Figure 5a) and Co_3O_4_Cu2 (Figure 5b) are in good accordance with pure Co_3O_4.[10,24] Cu-alloyed Co_3O_4_Cu2 nanowires exhibit an additional Cu $2p_{3/2}$ peak (~934.0 eV) and a shake-up peak at ~942.0 eV that is a characteristic peak of Cu^{2+} (Figure 5c). The atomic ratios of Cu/Co and Co^{2+}/Co^{3+} on the surface of the Co_3O_4_Cu*x* nanowires are further extracted from the XPS spectrum, and they are plotted as functions of the Cu/Co molar ratio in the precursor solution (Figure 5d). First, the Cu/Co atomic ratio on the surface of the Co_3O_4_Cu*x* nanowires clearly increases with that in the precursor solution, as expected, and the atomic ratios determined by XPS agree well with those measured by SEM-EDX. This observation is consistent with the STEM-EDX line profiles of Cu and Co (Figure 3f) in that the Cu alloying is quite uniform in the nanowires. Second, the Co^{2+}/Co^{3+} atomic ratio on the surface of the Co_3O_4_Cu*x* nanowires first decreases and then drastically increases with that in the precursor solution. The initial decrease in the Co^{2+}/Co^{3+} atomic ratio should be originating from the substitution of Cu^{2+} for Co^{2+} in Co_3O_4_Cu1 and Co_3O_4_Cu2. The further increase of the Co^{2+}/Co^{3+} atomic ratio for Co_3O_4_Cu3 is due to the formation of CoO and CuO phases according to the XRD results.

From the characterization results shown above, we know that Co_3O_4_Cu0 is pure Co_3O_4 without Cu; Co_3O_4_Cu1 and Co_3O_4_Cu2 are the desired modified Co_3O_4 for which Co^{2+} is substituted with Cu^{2+}; and Co_3O_4_Cu3 is a mixture of Co_3O_4, CuO, and CoO. It also should be noted that all four Co_3O_4_Cu*x* (x = 0, 1, 2, and 3) nanowires were grown on SS meshes with the same dimension, and they, according to the BET analysis, have comparable total mass loading, specific surface area, and total surface area (all without including the SS mesh) with <6% variation, as listed in Table 1. With all this information, we can directly compare their respective catalytic activity for CO oxidation, as shown in Figure 6a. First, Co_3O_4_Cu1 and Co_3O_4_Cu2 have a higher catalytic activity for CO oxidation than Co_3O_4_Cu0 for the entire tested temperature range of 60−120 °C. Co_3O_4_Cu2 has the highest catalytic activity among all four samples, and its CO conversion percentage nearly doubles that of sample Co_3O_4_Cu0 at some temperatures. These results indicate that substituting Co^{2+} with Cu^{2+} in these polycrystalline Co_3O_4 nanowires indeed greatly enhances their catalytic activity for CO oxidation, and the more substitution, the better provided

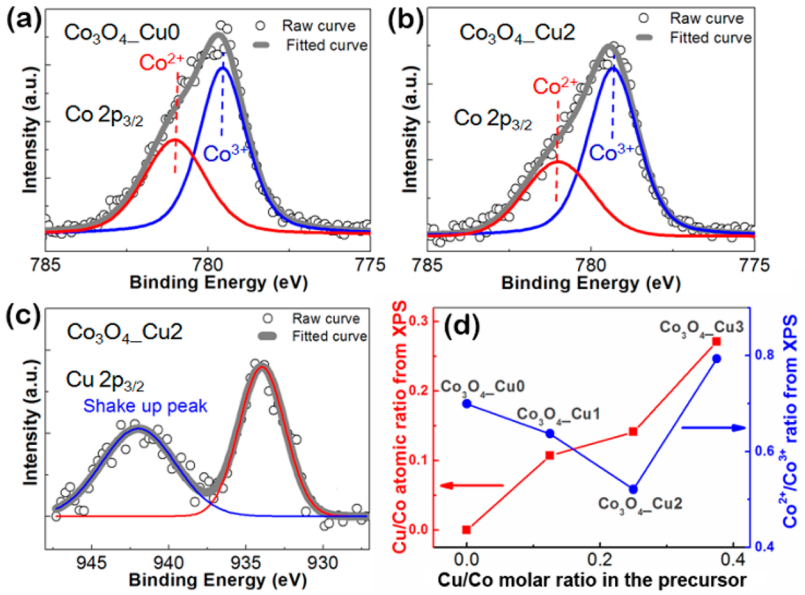

Figure 5. XPS spectra of the Co $2p_{3/2}$ peak for (a) Co_3O_4_Cu0 and (b) Co_3O_4_Cu2 nanowires, and (c) the Cu $2p_{3/2}$ peak for Co_3O_4_Cu2 nanowires; (d) the measured Cu/Co atomic ratio and Co^{2+}/Co^{3+} atomic ratio on the surface of the Co_3O_4_Cu*x* nanowires as a function of the Cu/Co molar ratio in the growth precursor solution.

DOI: 10.1021/acscatal.5b00488
ACS Catal. 2015, 5, 4485−4491

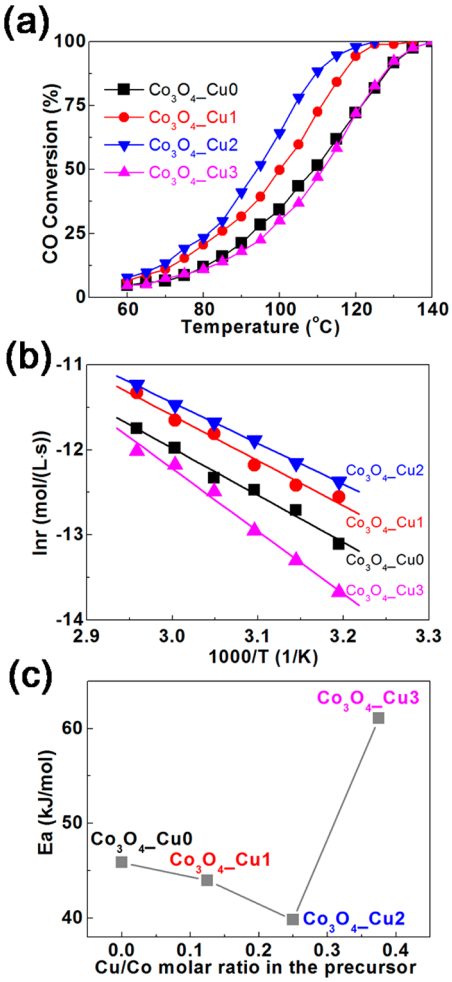

Figure 6. (a) CO conversion percentages over all the Co_3O_4_Cu*x* nanowires as a function of temperature; (b) Arrhenius plots for all the Co_3O_4_Cu*x* nanowires; (c) activation energies for all the Co_3O_4_Cu*x* nanowires as a function of the Cu/Co molar ratio in the growth precursor solution.

phase segregation is avoided. Second, Co_3O_4_Cu3 shows even poorer catalytic performance than that of a pure Co_3O_4 sample (Co_3O_4_Cu0) because of the presence of less-active CuO and CoO phases. Third, we extracted the activation energy from the Arrhenius plots[15] for all four samples (Figure 6b), in which the reaction rate of CO (r, mol/(L·s)) was expressed in the form of

$$r = -\frac{\mathrm{d}[\mathrm{CO}]}{\mathrm{d}t} = A\exp\left(-\frac{E_a}{RT}\right)[\mathrm{O_2}]^a[\mathrm{CO}]^b$$

where E_a is the activation energy (kJ/mol); A is the preexponential factor; and a and b are the reaction orders for O_2 and CO, respectively. The reaction temperature was chosen in the range of 40−65 °C to keep CO conversion below 15% for realizing a differential reactor assumption. As expected, the activation energy is inversely correlated to the CO conversion rate over Co_3O_4_Cu*x* nanowires (Figure 6c). Finally, to further evaluate our best Cu-alloyed sample (Co_3O_4_Cu2), we calculated its mass-specific conversion rate of CO at 65 °C that gives 10% CO conversion (T_{10}). The mass-specific conversion at T_{10} for Co_3O_4_Cu2 is 0.82 μmol g^{-1} s^{-1}, which is comparable to that of single crystalline Co_3O_4 nanobelts with predominantly exposed {110} planes (0.85 μmol g^{-1} s^{-1} at T_{10}).[11] Given the fact that our Co_3O_4_Cu2 nanowires are polycrystalline without any specific surface facet control, the comparable catalytic activity indicates that the current Cu^{2+} substitution method is as effective as the surface facet control strategy.

Previous theoretical studies[8,18,25,26] have investigated CO oxidation only on pure Co_3O_4 surfaces. To get a deeper insight into the enhanced effect of Cu^{2+} cations on the catalytic activity of the Co_3O_4_Cu*x* nanowires, we performed DFT+U calculations (see Supporting Information for details). First, the energetics of the low-index surfaces of pure Co_3O_4 were investigated as a function of the oxygen chemical potential (Figure 7a) using the procedure established by Reuter and Scheffler.[27] Calculations reveal that at experimentally relevant conditions (highlighted with the gray shaded area in Figure 7a),

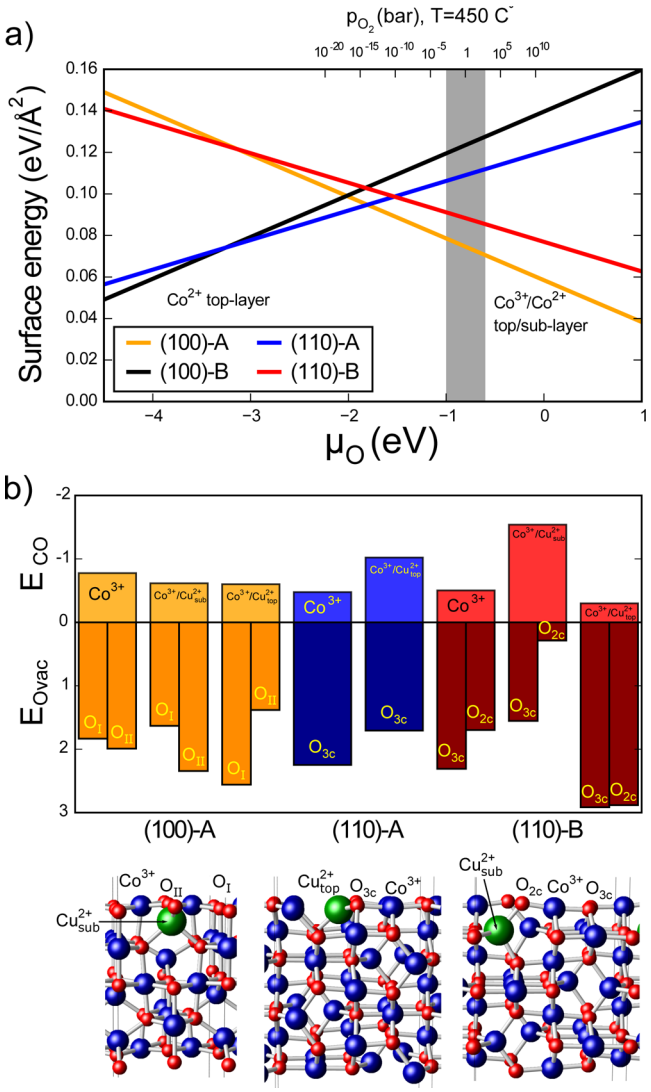

Figure 7. (a) Surface energies of the four low-index surfaces of spinel Co_3O_4 plotted as a function of oxygen chemical potential, μ_O. The shaded area highlights the relevant experimental conditions that show the most likely exposed surfaces in our nanowires are (100)-A, (110)-B, and (110)-A. (b) Calculated CO adsorption (upper bars) and oxygen vacancy formation energies (lower bars) for Cu-doped (100)-A, (110)-A, and (110)-B surfaces. Insets illustrate the atomistic side view of the corresponding unit cells: $p(\sqrt{2}\times\sqrt{2})$ for (100)-A and $p(1\times 1/2)$ for (110)-A/B are shown with labels indicating the considered metal adsorption sites and oxygen vacancy sites.

DOI: 10.1021/acscatal.5b00488
ACS Catal. 2015, 5, 4485−4491

the (100)-A, (110)-B, and (110)-A are the most stable surface terminations, in agreement with previous theoretical works.[8,28] For that reason, we limit our study of CO oxidation to the above three surface terminations.

Herein, we included a single-site doping of Co with Cu in the top-surface and subsurface layers of (100)-A, (110)-B, and (110)-A surfaces and identified the preferred Cu doping sites. This atomistic model is a good approximation for systems with low (<25%) substitution concentration. For all investigated surfaces, we find that Cu^{2+} is more stable when substituting a Co surface site in the top-surface layer compared with a subsurface substitution. On the (110)-A surface terminated with both Co^{2+} and Co^{3+}, the Cu substitution is preferred in the Co^{2+} site by 1.75 eV. The (110)-B and the (100)-A surfaces are both terminated with Co^{3+}, for which top-surface Cu doping is 0.72 and 0.56 eV, respectively, more stable than the subsurface doping.

To investigate the effect of Cu doping on the CO oxidation on Co_3O_4, we extended the study of Wang et.al.,[8] which showed that (a) only Co^{3+} exposed surface sites adsorb CO sufficiently strongly, (b) CO readily reacts with a lattice oxygen to form a CO_2* intermediate, and (c) the barrier to form an vacancy is the limiting step of this process. Hence, to model the surface activity of Cu-doped Co_3O_4, we calculate the CO adsorption energies and oxygen vacancy formation energies and omit the explicit calculations of barriers because these have been found to be correlated to the thermodynamic steps according to Brønsted−Evans−Polanyi relations.[29] The calculated CO adsorption energies, $E_{CO} = E_{CO+surf} - E_{surf} - E_{CO}$, and oxygen vacancy formation energies, $E_{Ovac} = E_{Ovac} - E_{surf} + (1/2)E_{O_2}$, as a function of Cu substitution sites are summarized in Figure 7b. Our results show that (a) CO adsorbs only on Co^{3+} and not on Co^{2+} or Cu^{2+}, regardless of the position of the Cu atom in the lattice; (b) the presence of Cu in Co_3O_4 strengthens the CO adsorption bond on the (110)-A/B surfaces and only slightly weakens it on the (100)-A surface; (c) depending on the type of vacancy (Figure 7b), we can identify one or more cases for each surface in which the oxygen vacancy formation becomes more favorable in the presence of Cu. The largest decrease in the vacancy formation energy was found for the O_{2c} vacancy on the Cu_{sub}^{2+}-doped (110)-B surface. There are two plausible reasons for the observed trends in the O vacancy formation energies due to the Cu dopant. One is related to the direct bond between O_{2c} and the Cu^{2+} dopant that has to be broken upon vacancy formation. The second one is the difference in electron localization around the vacancy. For undoped surfaces, we observe that the two electrons left are strongly localized on a single Co site, whereas for Cu-doped surfaces, the electrons are delocalized over several Co sites and therefore energetically more favorable.

CONCLUSIONS

In summary, we have investigated the effect of substituting Co^{2+} with Cu^{2+} on the catalytic properties of Co_3O_4 for CO oxidation through a complementary experimental and computational study. Cu-alloyed Co_3O_4_Cu*x* polycrystalline nanowires were synthesized using a modified hydrothermal method, and they exhibit much higher catalytic activity for CO oxidation than the pure Co_3O_4 nanowires. This activity enhancement increases up to an optimal amount of Cu^{2+} substitution for Co^{2+}. Moreover, these Cu-alloyed Co_3O_4_Cu*x* polycrystalline nanowires have catalytic activity for CO oxidation that is similar to single crystalline Co_3O_4 nanobelts with predominantly exposed most active {110} planes. Using atomic modeling, we find that Co^{3+} remains as the active sites for CO adsorption for Cu-doped Co_3O_4, and the Cu substitution affects the CO adsorption energies only slightly. Nonetheless, the oxygen vacancy is more favorably formed in the bonding of Co^{3+}−O−Cu^{2+} than in Co^{3+}−O−Co^{2+}, which leads to an enhancement in CO oxidation. We believe that the general strategy of isovalent-cation substitution opens up new opportunities for enhancing the catalytic activity for transition metal oxides.

ASSOCIATED CONTENT

Supporting Information

The Supporting Information is available free of charge on the ACS Publications website at DOI: 10.1021/acscatal.5b00488.

DFT+U calculation details (PDF)

AUTHOR INFORMATION

Corresponding Authors

*E-mail: xlzheng@stanford.edu.

*E-mail: wuweidongding@163.com.

Author Contributions

⊥M.Z. and L.C. contributed equally to this work.

Notes

The authors declare no competing financial interest.

ACKNOWLEDGMENTS

M. J. Zhou sincerely thanks the support from National Natural Science Foundation of China (NSFC, Grant No. 11104256) and China Scholarship Council (CSC, Grant No. 201204890001). X. L. Zheng sincerely thanks the support from the ONR/PECASE program. M. Bajdich, M. García-Melchor, and A. Vojvodic thank the support from the U.S. Department of Energy Office of Basic Energy Science to the SUNCAT Center for Interface Science and Catalysis.

REFERENCES

(1) Royer, S.; Duprez, D. *ChemCatChem* **2011**, *3*, 24−65.

(2) Fu, Q.; Yang, F.; Bao, X. *Acc. Chem. Res.* **2012**, *3*, 1692−1701.

(3) Liu, X. Y.; Liu, M. H.; Luo, Y. C.; Mou, C. Y.; Lin, S. D.; Cheng, H. K.; CHen, J. M.; Lee, J. F.; LIn, T. S. *J. Am. Chem. Soc.* **2012**, *134*, 10251−10258.

(4) Xie, S. H.; Dai, H. X.; Deng, J. G.; Liu, Y. X.; Yang, H. G.; Jiang, Y.; Tan, W.; Ao, A. S.; Guo, G. S. *Nanoscale* **2013**, *5*, 11207−11219.

(5) Grillo, F.; Natile, M. M.; Glisenti, A. *Appl. Catal., B* **2004**, *48*, 267−274.

(6) Yu, Y. B.; Takei, T.; Ohashi, H.; He, H.; Zhang, X. L.; Haruta, M. *J. Catal.* **2009**, *267*, 121−128.

(7) Liotta, L. F.; Wu, H. J.; Pantaleo, G.; Venezia, A. M. *Catal. Sci. Technol.* **2013**, *3*, 3085−3102.

(8) Wang, H. F.; Kavanagh, R.; Guo, Y. L.; Guo, Y.; Lu, G.; Hu, P. *J. Catal.* **2012**, *296*, 110−119.

(9) Xie, X. W.; Li, Y.; Liu, Z. Q.; Haruta, M.; Shen, W. J. *Nature* **2009**, *458*, 746−749.

(10) Petitto, S. C.; Marsh, E. M.; Carson, G. A.; Langell, M. A. *J. Mol. Catal. A: Chem.* **2008**, *281*, 49−58.

(11) Hu, L. H.; Sun, K. Q.; Peng, Q.; Xu, B. Q.; Li, Y. D. *Nano Res.* **2010**, *3*, 363−368.

(12) Sun, Y.; Lv, P.; Yang, J. Y.; He, L.; Nie, J. C.; Liu, X. W.; Li, Y. D. *Chem. Commun.* **2011**, *47*, 11279−11281.

(13) Lv, Y. G.; Li, Y.; Shen, W. J. *Catal. Commun.* **2013**, *42*, 116−120.

(14) Li, Y. G.; Zhu, L. P.; Guo, Y. M.; Jiang, J.; Hu, L.; Wen, Z.; Sun, L. W.; Ye, Z. Z. *ChemCatChem* **2013**, *5*, 3576−3581.

(15) Feng, Y. Z.; Zheng, X. L. *Nano Lett.* **2010**, *10*, 4762−4766.

DOI: 10.1021/acscatal.5b00488
ACS Catal. 2015, 5, 4485−4491

(16) Feng, Y. Z.; Rao, P. M.; Kim, D. R.; Zheng, X. L. *Proc. Combust. Inst.* **2011**, *33*, 3169−3175.
(17) Jansson, J. *J. Catal.* **2000**, *194*, 55−60.
(18) Broqvist, P.; Panas, I.; Persson, H. *J. Catal.* **2002**, *210*, 198−206.
(19) Lou, Y.; Ma, J.; Cao, X.; Wang, L.; Dai, Q.; Zhao, Z.; Cai, Y.; Zhan, W.; Guo, Y.; Hu, P.; Lu, G.; Guo, Y. *ACS Catal.* **2014**, *4*, 4143−4152.
(20) Pollard, M. J.; Weinstock, B. A.; Bitterwolf, T. E.; Griffiths, P. R.; Piers Newbery, A.; Paine Iii, J. B. *J. Catal.* **2008**, *254*, 218−225.
(21) Lou, Y.; Wang, L.; Zhao, Z.; Zhang, Y.; Zhang, Z.; Lu, G.; Guo, Y.; Guo, Y. *Appl. Catal., B* **2014**, *146*, 43−49.
(22) Chen, T.; Li, X. W.; Qiu, C. C.; Zhu, W. C.; Ma, H. Y.; Chen, S. H.; Meng, O. *Biosens. Bioelectron.* **2014**, *53*, 200−206.
(23) Shirley, D. A. *Phys. Rev. B* **1972**, *5*, 4709−4714.
(24) Zhu, J. J.; Kailasam, K.; Fischer, A.; Thomas, A. *ACS Catal.* **2011**, *1*, 342−347.
(25) Xu, X.-L.; Yang, E.; Li, J.-Q.; Li, Y.; Chen, W.-K. *ChemCatChem* **2009**, *1*, 384−392.
(26) Jiang, D.-E.; Dai, S. *Phys. Chem. Chem. Phys.* **2011**, *13*, 978−984.
(27) Reuter, K.; Scheffler, M. *Phys. Rev. B: Condens. Matter Mater. Phys.* **2001**, *65*, 035406.
(28) Chen, J.; Selloni, A. *Phys. Rev. B: Condens. Matter Mater. Phys.* **2012**, *85*, 085306.
(29) Vojvodic, A.; Calle-Vallejo, F.; Guo, W.; Wang, S.; Toftelund, A.; Studt, F.; Martínez, J. I.; Shen, J.; Man, I. C.; Rossmeisl, J.; Bligaard, T.; Nørskov, J. K.; Abild-Pedersen, F. *J. Chem. Phys.* **2011**, *134*, 244509.

DOI: 10.1021/acscatal.5b00488
ACS Catal. 2015, 5, 4485−4491